Electronic Supplementary Material (ESI) for Journal of Materials Chemistry A.

High-Performance Fully-Stretchable Solid-State Lithium-Ion Battery with Nanowire-Network Configuration and Crosslinked Hydrogel (Supporting Information)

1. Fabrication of Ag-nanowire networks

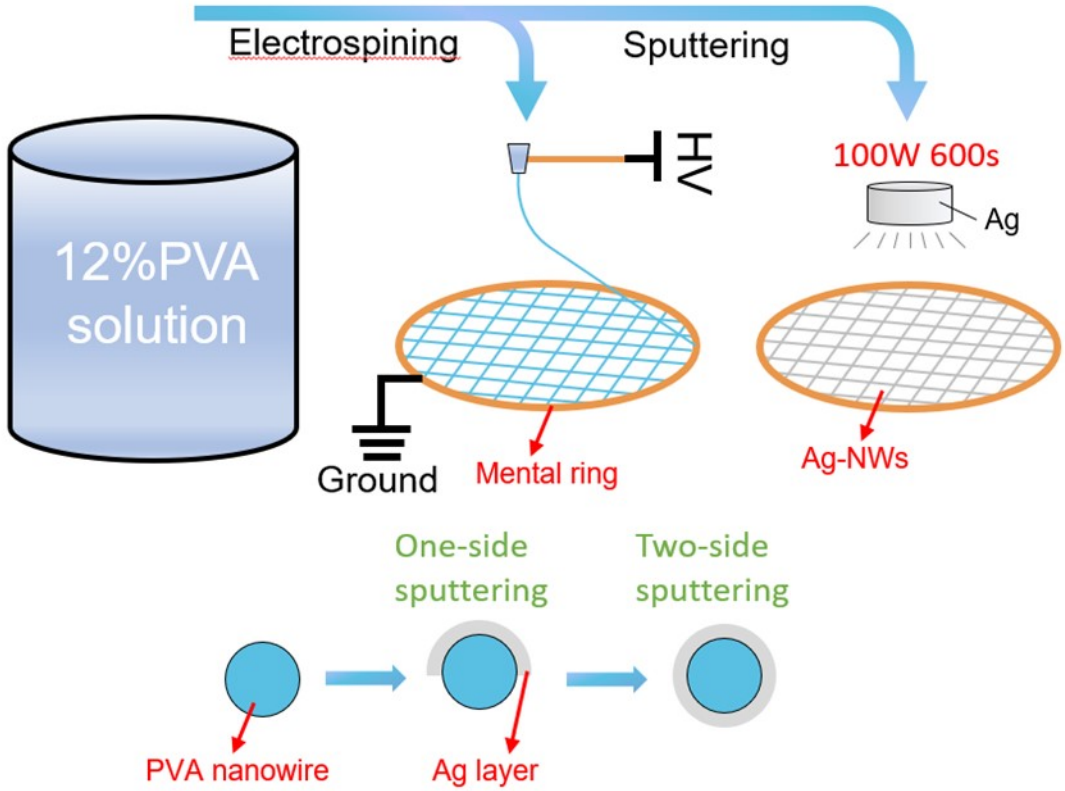

Figure S1. Schematic diagrams for the fabrication of Ag-nanowire networks.

Preparation of the Ag-NW network structure are as followed: As shown in upper inset of Fig. S1, the precursor solution with mass fraction concentration of 12% was prepared by dissolved 1.36 g of PVA (Poly (vinyl alcohol), MW 1788) into 10 mL of deionized water, followed by the heating and stirring process, lasting for 24 h, at 80°C and 2000 rpm respectively. Then the cooled PVA precursor was injected into a syringe connected to a

mental spinning nozzle, 1.05 mm diameter, by a long and thin hose and a precision stepper driver, where the stepper driver ensures that PVA solution can be extruded through the spinning nozzle at an accurate and stable rate for continuous wire drawing. A high voltage (about 10.58 kV) was applied between the mental nozzle (positive electrode) and the mental receiving ring (negative electrode) for forming a high electric field, where the distance between the positive and negative electrode is set to about 6 cm. In the electrostatic-spinning process, PVA aqueous solution beads formed abundant fine nanowires under the action of electric field, which are collected by the mental receiving ring and interconnected into a complete network. The sparse density of the PAV-nanowire network depends on the electrostatic-spinning time. Finally, as shown in lower schematic diagrams of Fig. S1, a uniform layer of Ag (operating power of 100W, sputtering time of 600s) were deposited on the PAV-nanowires through magnetron sputtering technique (K.J. Lesker PVD 75). During the depositing process, the conductive Ag were firstly deposited on one side of the PVA nanowires and then the Ag layer was deposited by

magnetron sputtering on the other side to obtain complete Ag-nanowire network. Ag-nanowire network prepared on the basis of interconnected PVA nanowire framework not only has excellent conductivity but also is not easy to be damaged in the bended and twisted deformations.

2. Morphology comparison for the AM islands/nanowires interconnected configure

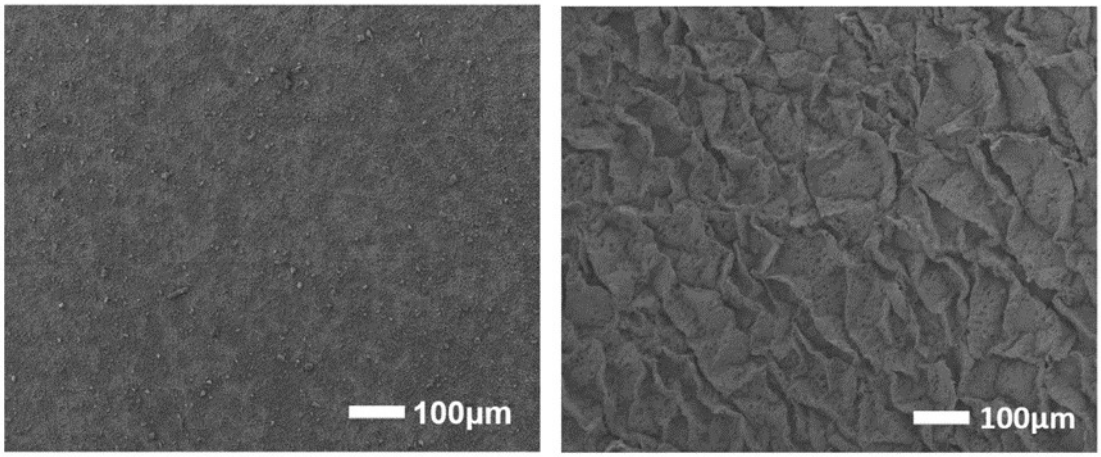

Figure S2. Top-view SEM images of AM islands/nanowires interconnected configure. AM islands dispersed on the hollowed structure nanowire networks before transferring to the hydrogel electrolyte (left) and the transferred CANN supported AM-islands configuration (right).

The AM blocks loaded on the supple Ag-Nanowires, forming the dispersed island interconnection structure, are pressed on both side of the pre-stretching PAM-electrolyte as cathode and anode. The Ag-nanowires independently supported AM islands allows the mechanical strain to be distributed on the softer nanowires instead of the stiffer and fragile AM.

3. Elemental mapping analysis of the AM islands/nanowires interconnected configure

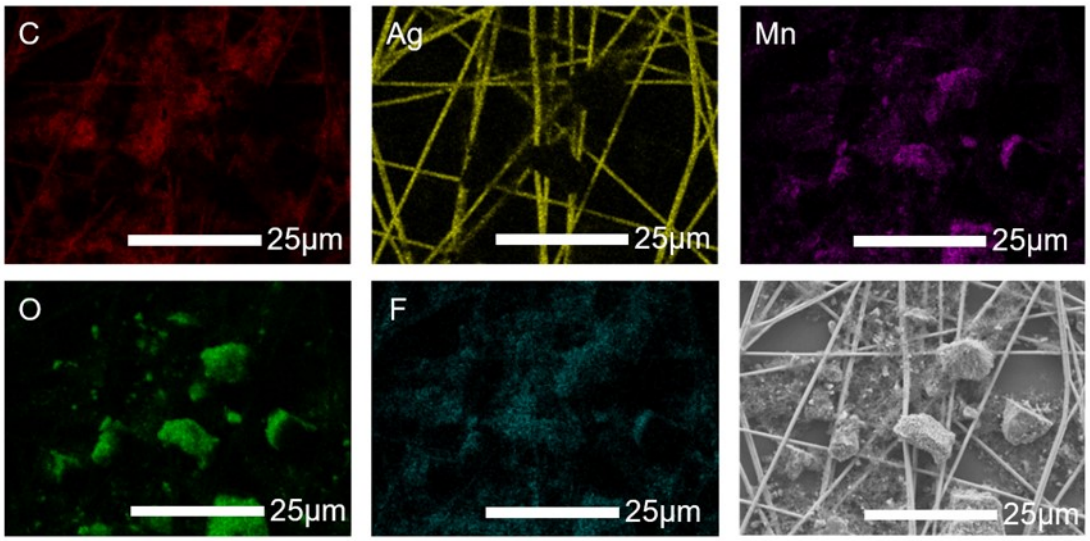

Figure S3. Energy Dispersive Spectroscopy (EDS) elemental mapping of the LMO/CB/Ag-nanowires.

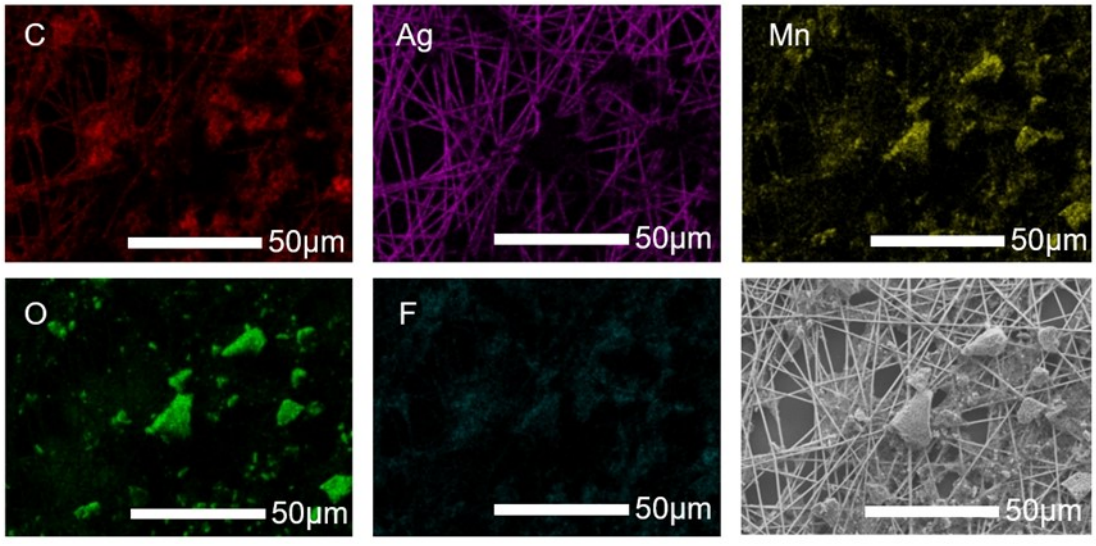

Figure S4. EDS elemental mapping analysis of the LMO/CB/CANN cathode after stretching process.

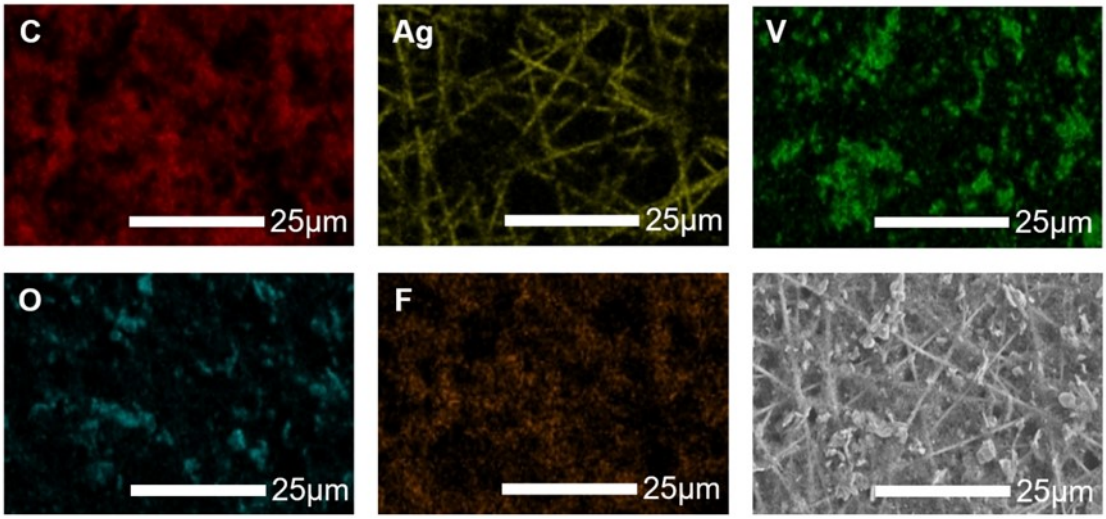

Figure S5. Energy Dispersive Spectroscopy (EDS) elemental mapping of the V_2O_5/CB/Ag-nanowires.

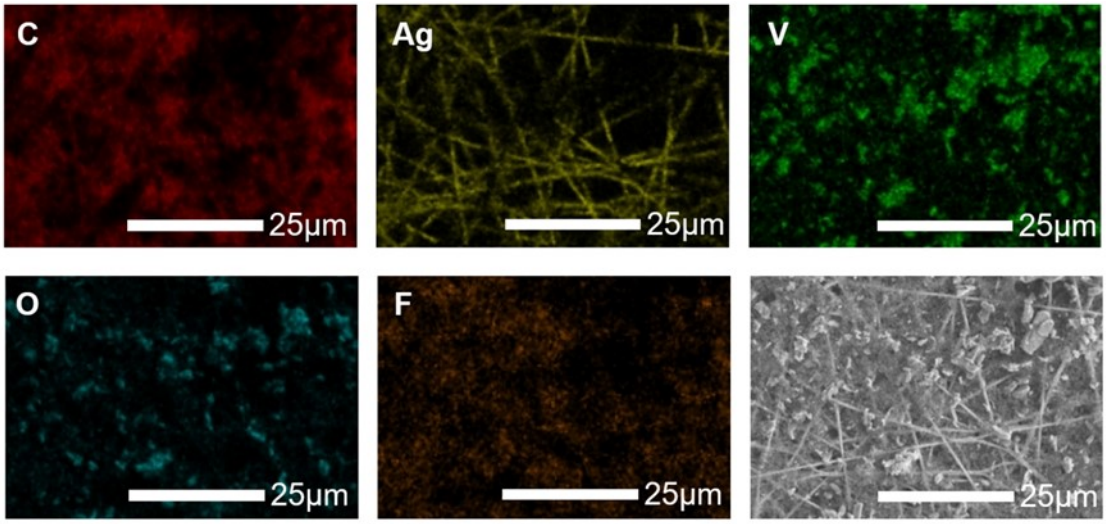

Figure S6. EDS elemental mapping analysis of the V_2O_5/CB/CANN anode after stretching process.

According to the EDS elemental mapping analyses of anode and cathode, the conductive agent and active materials of anode and cathode are uniformly dispersed on

the Ag-nanowires, where fluorine element is derived from the binder PVDF. In addition, after the CANN cathode and CANN anode were stretched, the active materials were still uniformly dispersed on the CANN.

4. Morphology evolution comparison for CANN electrodes

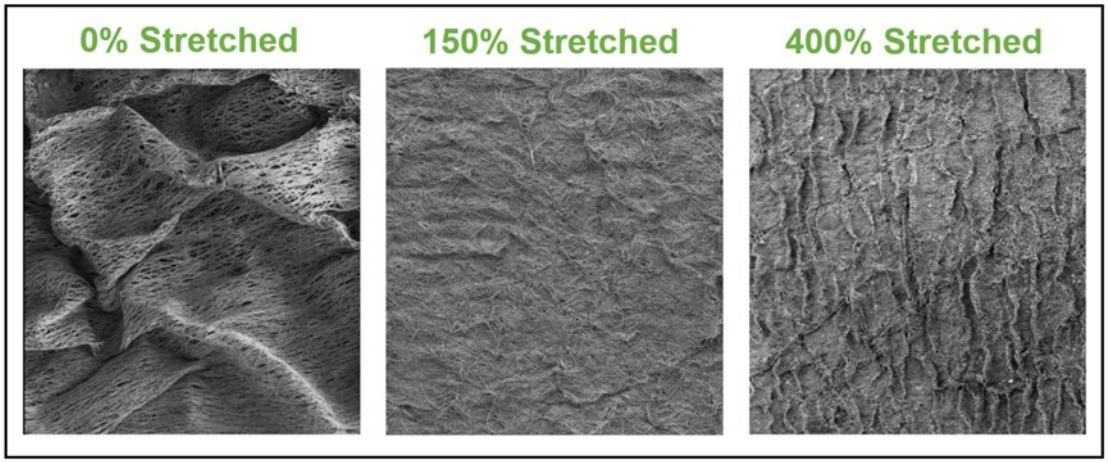

Figure S7. Top-view SEM images of the morphology evolution of CANN electrodes covered on the PAM hydrogel with the increasing stretching strain.

When the stretching strain increases from 0% to about 200%, the wrinkled nanowires in the stretching direction actually evolve towards planarization forming less tangled junctions, whereas the wrinkled nanowires perpendicular to the stretching direction tends to transform to a relatively more wrinkled state to a certain degree, accompanying with the decreasing conductivity of the CANN electrodes. When the externally applied stretching strain is far more than 200%, the measured Rs remains extremely stable conductivity without any significant fluctuations, which

indicated that the vertical aggregation of the crumpling evolution nanowires ensures stable electrical properties of the CANN, accompanying with a slightly increase of conductivity.

5. The aspect ratio of PAM hydrogel substrate

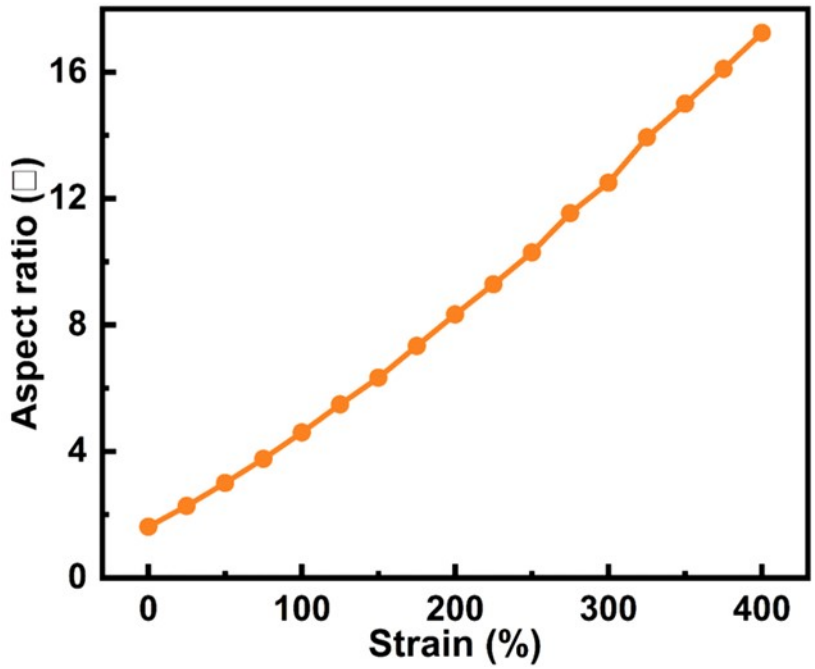

Figure S8. Changes of the aspect ratio of PAM hydrogel substrate with the increase of the stretching strain.

The aspect ratio of PAM hydrogel substrate under 0% - 400% stretching strain is to increase sharply with the increase of strain. The trend of the measured Rs at 1st and 50th cycles with increasing after decreasing (Fig. 2d) illustrates that the increase of the electrode aspect ratio far exceeds the stretching loss of surface resistance of the CANN electrode, where the CANNs go through complicated morphological evolution during the stretching process.

6. Electrical performance of the CANN collector.

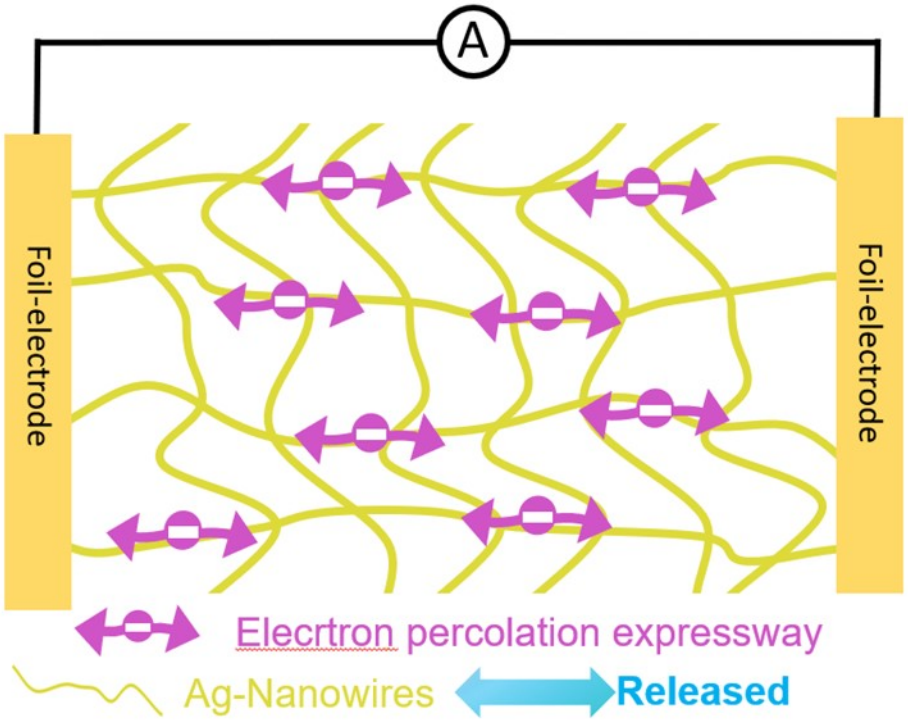

Figure S9. Schematic diagrams of the electron transport mechanism of the CANN collector at 0% stretching strain.

As shown in Fig. S5, the applied external current will form an electric field in the plane of the current collector along the stretching direction, and the electrons transport along the Ag-nanowires in the stretching direction to form shortest percolation expressway with lowest resistance in the unstretched state.

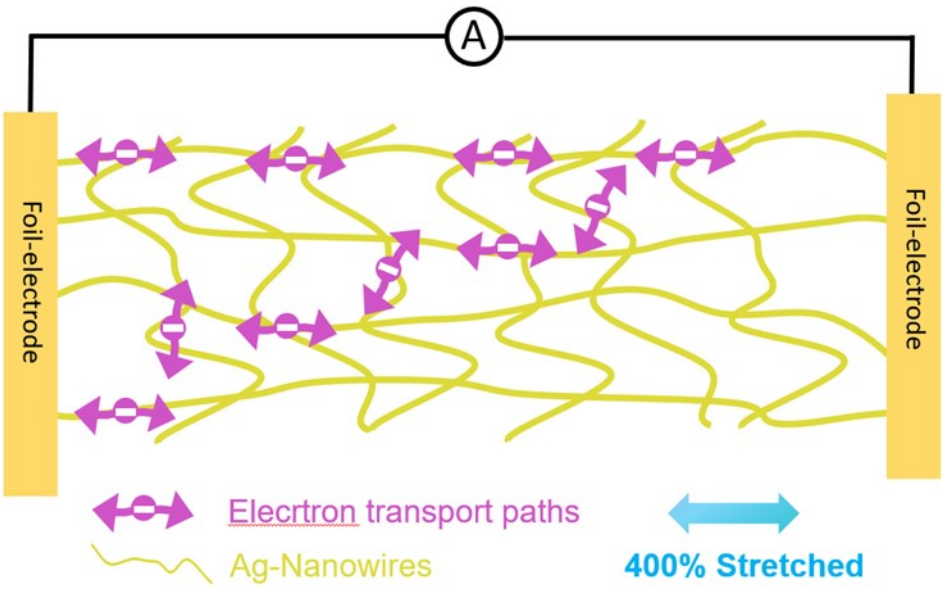

Figure S10. Schematic diagrams of the electron transport paths of the CANN collector with extensive broken nanowires at 400% stretching strain.

At the 400% stretching strain, an in-plane electric field of the current collector generated by the applied external current will still form along the stretching direction accompanying by more tangled junctions, as shown in Fig. S6, the crumpling evolution nanowires that are perpendicular to the stretch direction aggregate forming a more wrinkled state. The electrons will transport along the multiple paths with low resistance in a large extent of stretched state.

Table 1. Surface resistance of the Ag-NW CANN under different stretching strain at 1st stretching cycles.

Strain / R_s	0%	50%	100%	150%	200%	250%	300%	350%	400%	450%	500%
Stretching	0.99284	2.3008	2.0158	2.8858	2.55	2.1966	1.9469	3.3389	4.4657	4.1093	4.1606
Releasing	1.25757	2.48785	2.72668	3.2738	3.7852	4.481	5.4241	8.7587	7.8328	6.0717	4.1606

Table 2. Surface resistance of the Ag-NW CANN under different stretching strain at 50th stretching cycles.

Strain / R_s	0%	50%	100%	150%	200%	250%	300%	350%	400%	450%	500%
Stretching	0.9044	1.46448	2.2386	1.911	2.2275	3.3881	4.6068	6.3808	7.6524	7.0012	6.6189
Releasing	1.35387	2.7304	3.2979	3.9523	4.2761	5.5999	6.0715	5.7353	6.3669	6.7638	6.6189

Table 3. Surface resistance of the Ag-NW CANN under different stretching strain at 100th stretching cycles.

Strain / R_s	0%	50%	100%	150%	200%	250%	300%	350%	400%	450%	500%
Stretching	1.11455	1.46385	3.6018	7.5835	10.1974	8.8777	8.9094	10.1416	7.5057	8.3094	7.2528
Releasing	1.32984	1.8154	2.8568	3.3361	4.348	7.4062	7.4062	10.4865	9.2892	8.5234	7.2528

7. Mechanical properties characterization of PAM-CANN electrodes and PAM-WiS electrolyte

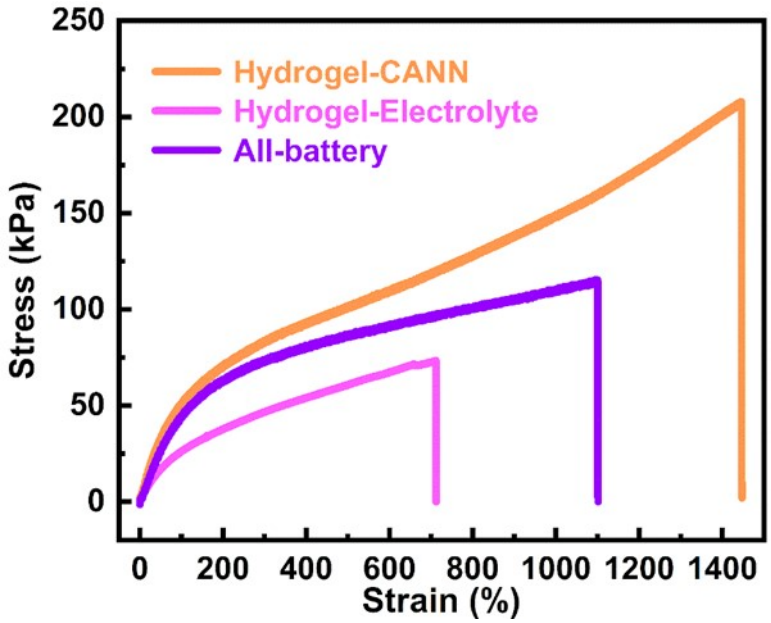

Figure S11. Stress-strain curves of the PAM-CANN electrode, the PAM-WiS electrolyte, and the assembled battery.

The stretchable PAM-CANN electrodes can be stretched to 1400 % of their original lengths, and the strain of the PAM-WiS electrolytes only can be reached to 700 % (the stretched images of the PAM-WiS electrolyte are shown in Fig. 3a of the main text). The elastic modulus of PAM-CANN is about 69.12 kPa, and the elastic modulus of PAM-WiS electrolyte is 38.4 kPa. The mechanical properties of all battery are between PAM-WiS electrolyte and PAM-CANN. All battery can be stretched to 1000 %

of its original length, and the elastic modulus is about 52 kPa.

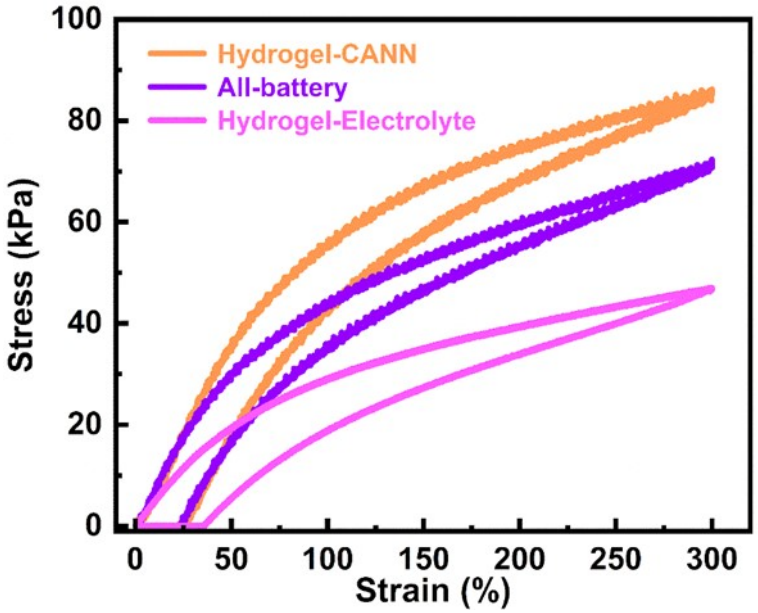

Figure S12. Stress-strain curves during loading–unloading process of the PAM-CANN electrode, the PAM-WiS electrolyte, and the assembled battery.

The loading–unloading tensile experiments were carried within 300% strain, the PAM-CANN and PAM-WiS electrolyte both exhibit large hysteresis and the energy dissipations, which are the main components of the energy dissipation during deformation of the whole battery.

8. Electrochemical characterization of the PAM-WiS electrolyte

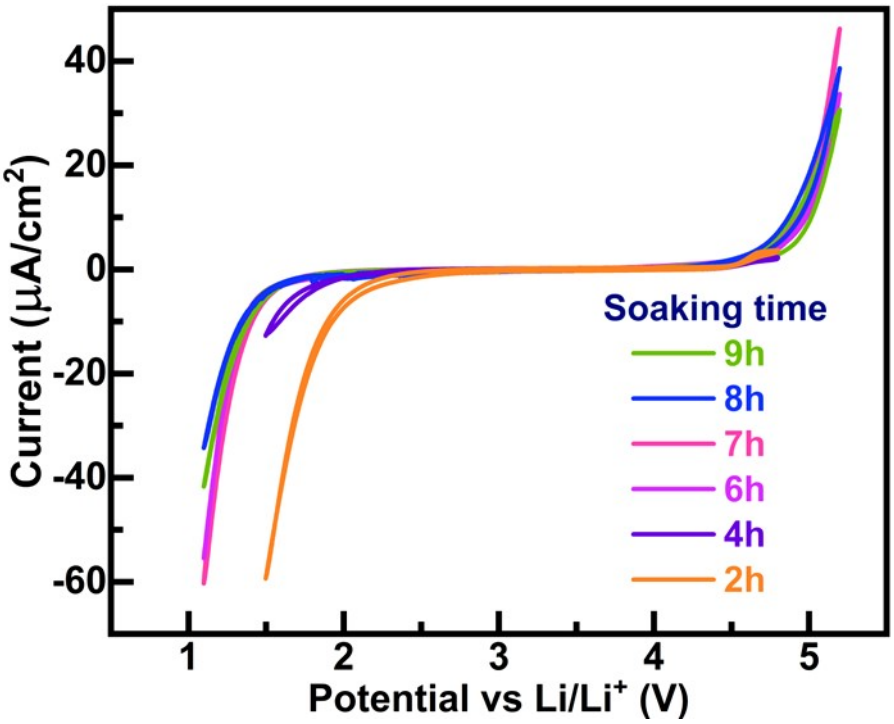

Figure S13. Electrochemical stable window of the PAM-WiS electrolyte with different soaking times.

Electrochemical stable window of the PAM-WiS electrolyte broaden with soaking times, and the stability window changes slightly when the soaking time is more than 6 h.

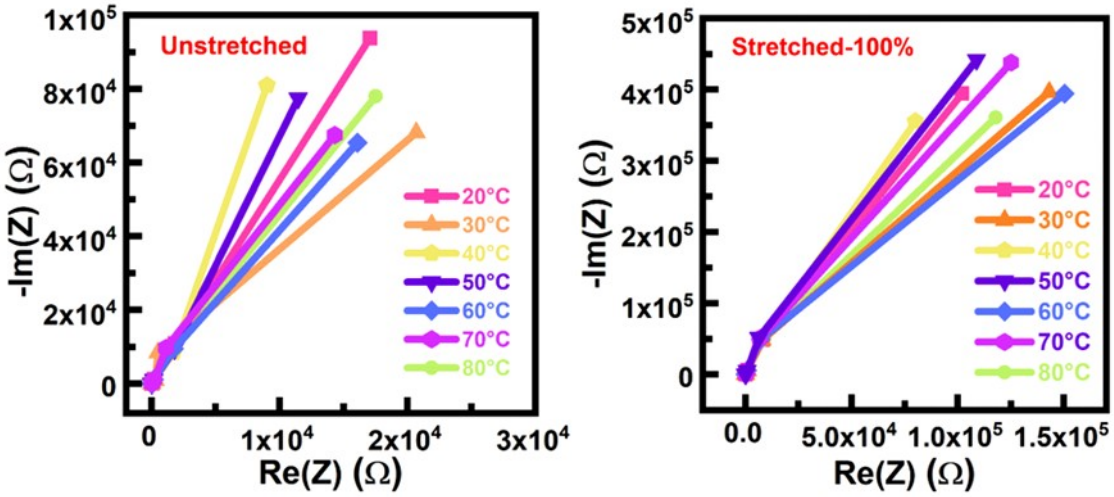

Figure S14. Nyquist plots of the PAM-WiS electrolyte at various temperatures.

The quasi-linear Nyquist plots with large Warburg impedance slope indicate that the Li^+ ion transfer processes of hydrogel electrolyte are dominated by diffusion control accompanying with an extremely low charge transfer impedance, where the electrolyte with higher impedance slope exhibits better performance from 20℃ to 50℃ and the electrolyte under stretched state possesses slightly lower impedance slope represent its superior stretching stability. Moreover, the impedance plural planar graph of the hydrogel electrolyte soaked for 6 hours with/without stretching strain at a measurement temperature of 20 ~ 80 ℃ are shown in Fig. S8.

9. Calculation of ionic transfer number

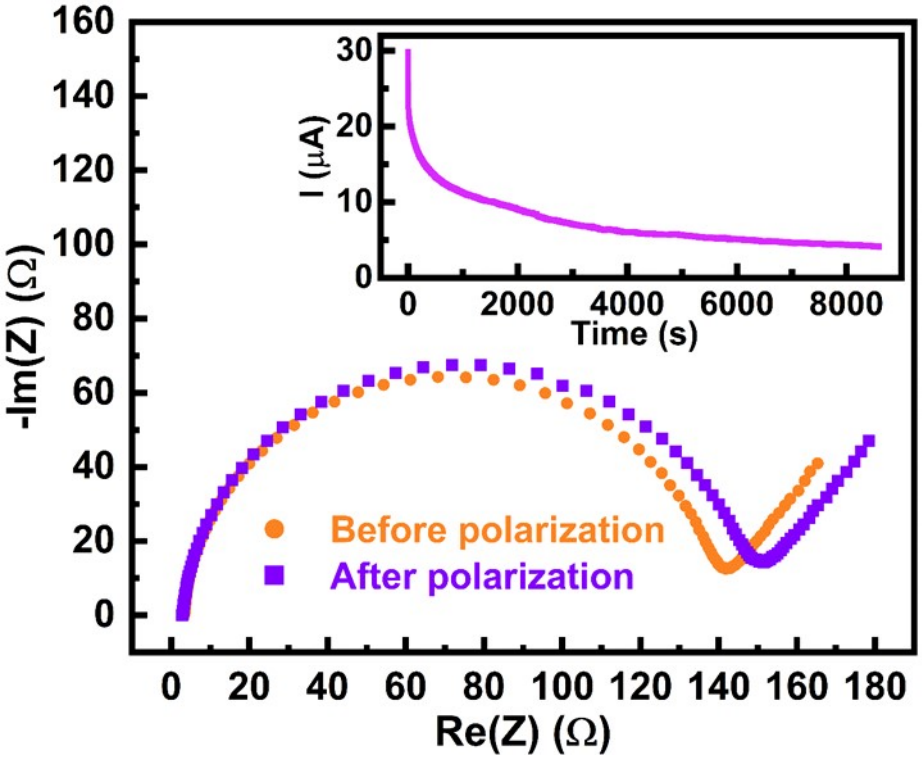

Figure S15. Steady-state current measurements and impedance spectrum before and after polarization of the PAM-WiS electrolyte.

The impedance spectrum before and after polarization of the PAM-WiS electrolyte (the frequency ranging from 100 mHz to 1 MHz) and the steady-state polarization current measurement (constant potential of 10 mV) are conducted by $LiMn_2O_4$/ PAM-WiS/$LiMn_2O_4$ symmetrical battery. And the ionic transfer number (t_{Li+}) can be calculated by the following expression [11]:

$$t_{Li^+} = \frac{I^s(\Delta v - I^0 R^0)}{I^0(\Delta v - I^s R^s)}$$

where I^0 and I^s are the currents in the polarized and unpolarized states respectively, while ΔV is the potential difference used in the test (10 mV). R^0 and R^s are the interface resistance before and after polarization in the symmetrical battery, respectively (diameter of the semicircular part of impedance spectrum).

According to Fig. S15, the ionic transfer number of the PAM-WiS electrolyte is

$$t_{Li^+} = \frac{I^s(\Delta v - I^0 R^0)}{I^0(\Delta v - I^s R^s)} = \frac{0.0041 \times (10 - 0.0298 \times$$
$$= 0.086$$

The result shows that the PAM-WiS electrolyte possesses the ionic transfer number of 0.086.

10. Characterization of the foil-collector un-stretchable cells

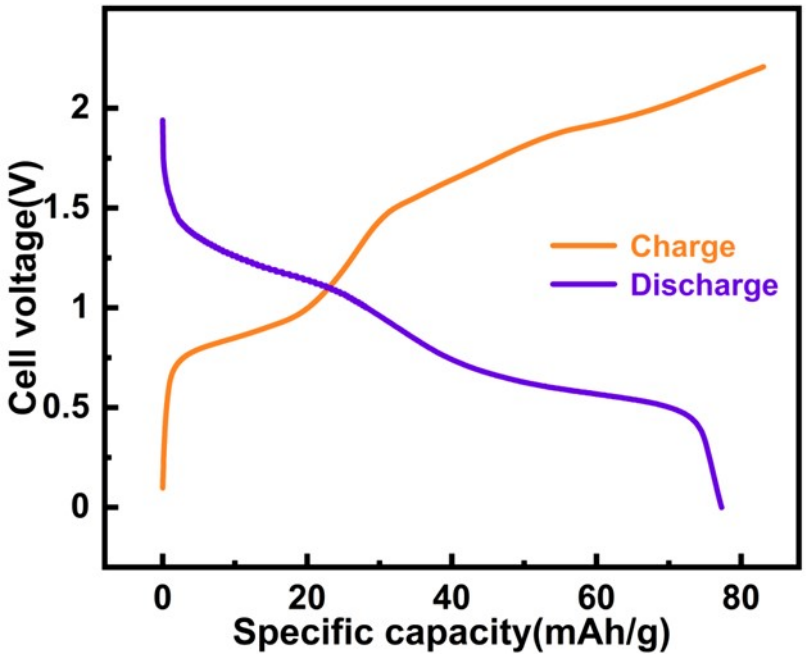

Figure S16. Voltage-capacity profile of the foil-collector un-stretchable cells, which is measured through GCPL: charge voltage-capacity profile (orange) and discharge voltage-capacity profile (purple).

Measured by galvanostatic cycling with potential limitation (GCPL), the un-stretchable full battery provides a stable discharge capacity of 80 mAh/g with two discharge platforms at about 1.5 V and 0.7 V, where the cathode and anode are prepared by spaying-coating LMO and V_2O_5 slurries onto aluminum foil and copper foil respectively (the voltage-specific capacity curve are

shown in Fig. S8). And the test results of capacity durability and Coulombic efficiency of the un-stretchable full battery displayed in Fig. S9 are that the battery possesses a steady capacity attenuation of 0.3% with a Coulombic efficiency of 90% at a rate of 1 C over 80 cycles, which confirms the feasibility of active materials and hydrogel electrolyte.

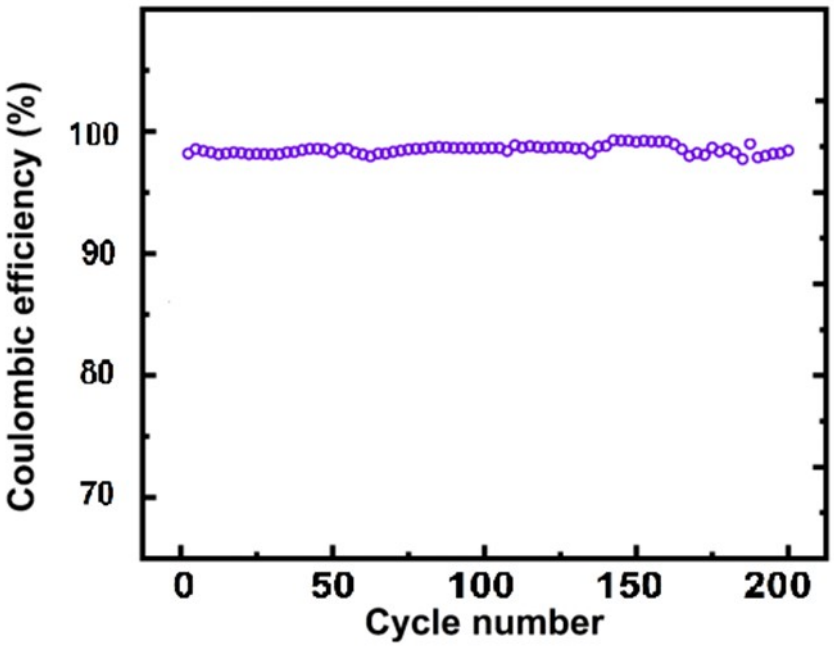

Figure S17. Cycling performance of the foil-collector un-stretchable cells for 80 cycles and the corresponding Coulombic efficiency at a current density of 60 mAg-1.

The un-stretchable battery possesses a steady capacity attenuation of 0.3% with a Coulombic efficiency of 90%

at a rate of 1 C over 80 cycles, which confirms the feasibility of active materials and hydrogel electrolyte.

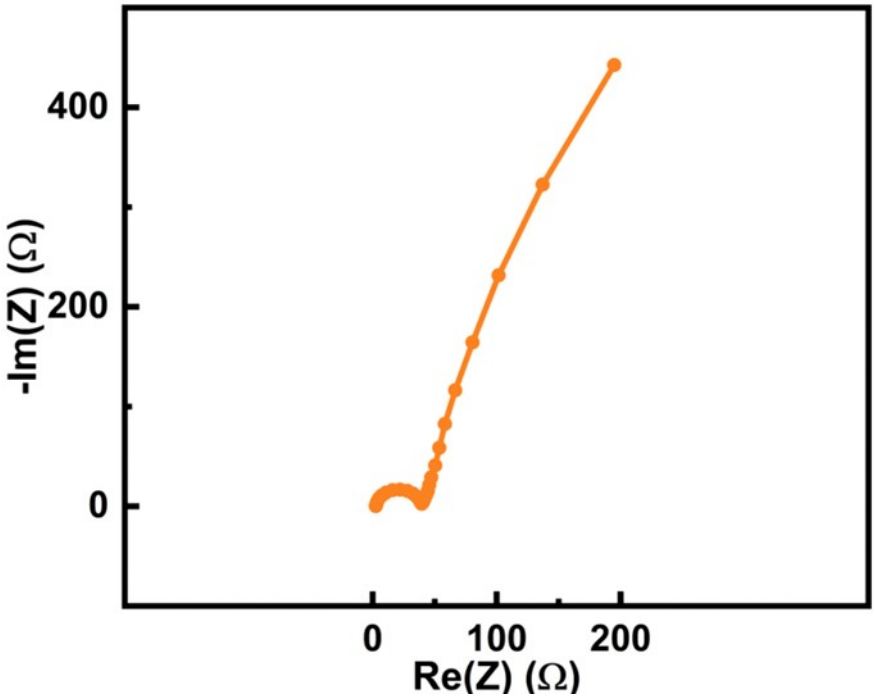

Figure S18. Nyquist plots of the foil-collector un-stretchable cell.

The extremely high specific capacity of the stretchable battery is even unexpectedly higher than that of the unstretched battery prepared by sandwiching the hydrogel electrolyte between anode and cathode that are prepared by spaying-coating active material slurry onto copper and aluminum foil, which is due to the acceleration of electronic and ionic transport through the AM islands dispersed on the porous network composed of one-

dimensional nanowires with extremely high specific surface area and buffering function of the volume change during charge and discharge.

11. Adhesion test of the electrode/electrolyte interface

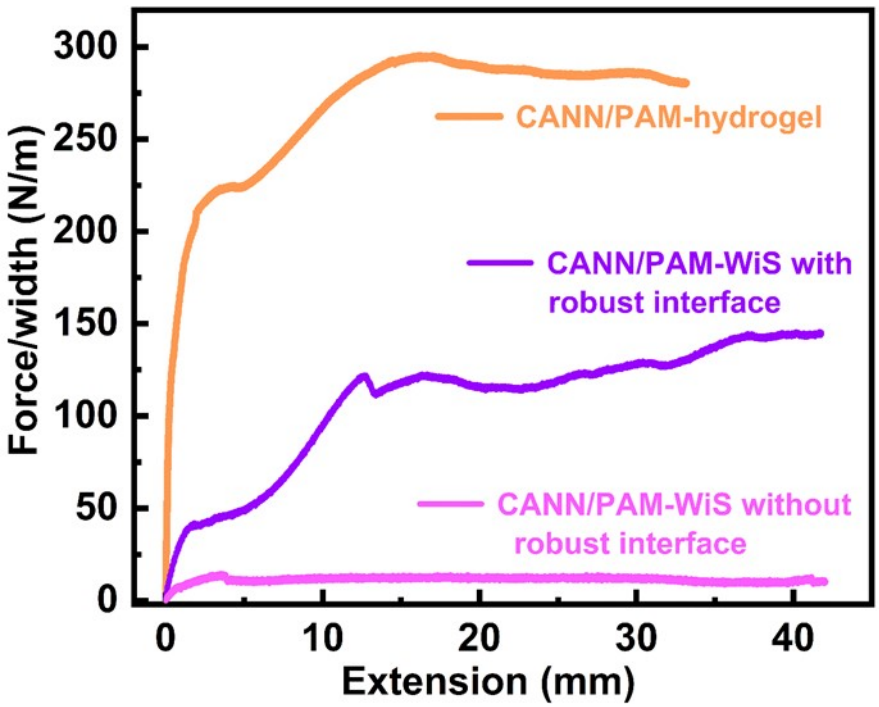

Figure S19. The adhesion test of the CANN/PAM-hydrogel cross-linked interface, the electrode/electrolyte fused interface, and the electrode/electrolyte stacked interface.

The adhesion energy can be obtained by the followed calculation formula [2]:

$$E = \frac{2F}{d}$$

where F is the peeled force during the adhesion test, and d is width of the interface.

According the adhesion test of the CANN/PAM-hydrogel cross-linked interface, the electrode/electrolyte fused

interface, and the electrode/electrolyte stacked interface, the adhesion energy of the fused interface (590 J/m2) is larger than that of the CANN/PAM-hydrogel robust interface (290 J/m2), which are both much larger than the adhesion energy of the CANN/PAM-WiS without robust interface (28 J/m2). The interface compatibility plays an important role in the excellent electrochemical performance of the FSSLIB.

12. Capacity per area and volume of the FSSLIB

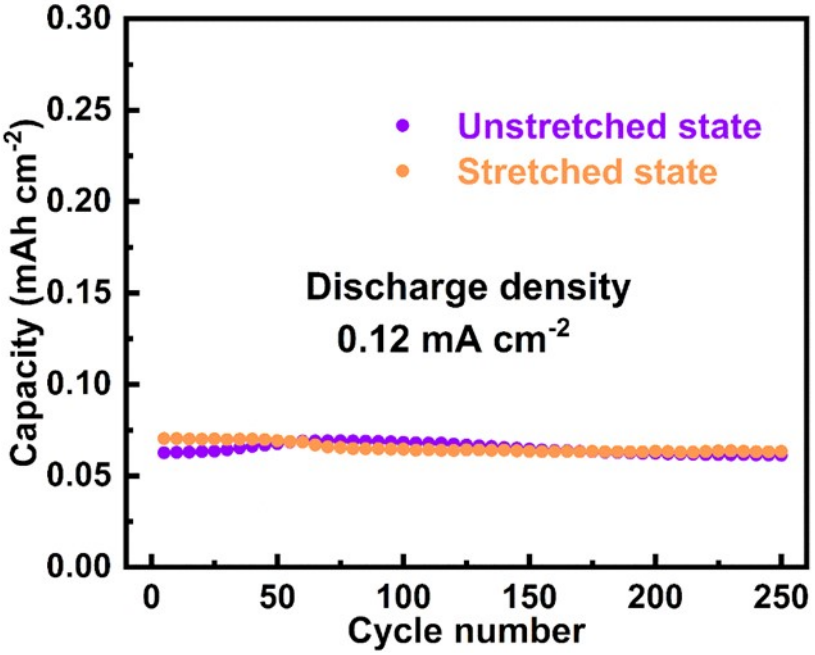

Figure S20. The discharge capacity per unit area during stretching cycles, with 0.12 mAh cm^{-2} current density.

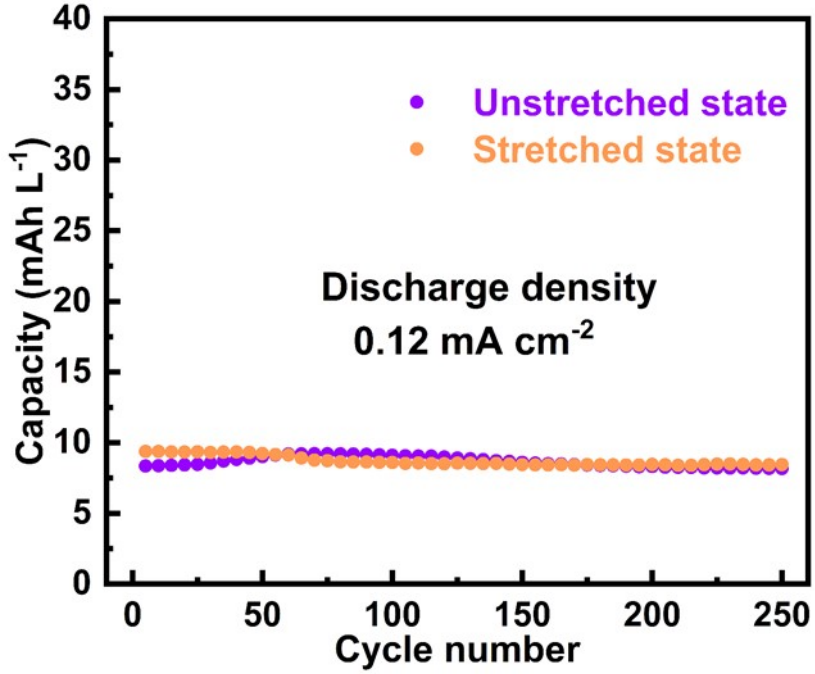

Figure S21. The discharge capacity per unit volume during stretching cycles.

The mass proportion of each CANN electrode with 34% is actually large, about 4.6 g (5x3x0.3 cm^3) of each current collector. And the weight of PAM-WiS electrolyte with anode and cathode is about 3.4 g (3x3x0.3 cm^3, accounting for 25%) and the packaging material weighs about 0.8 g (~0.65 cm^3). The FSSLIB focuses on the electrochemical performance under the stretched state, so the weight proportion of the component without active materials in the stretchable battery is relatively high.

13. Energy density of the stretchable cell

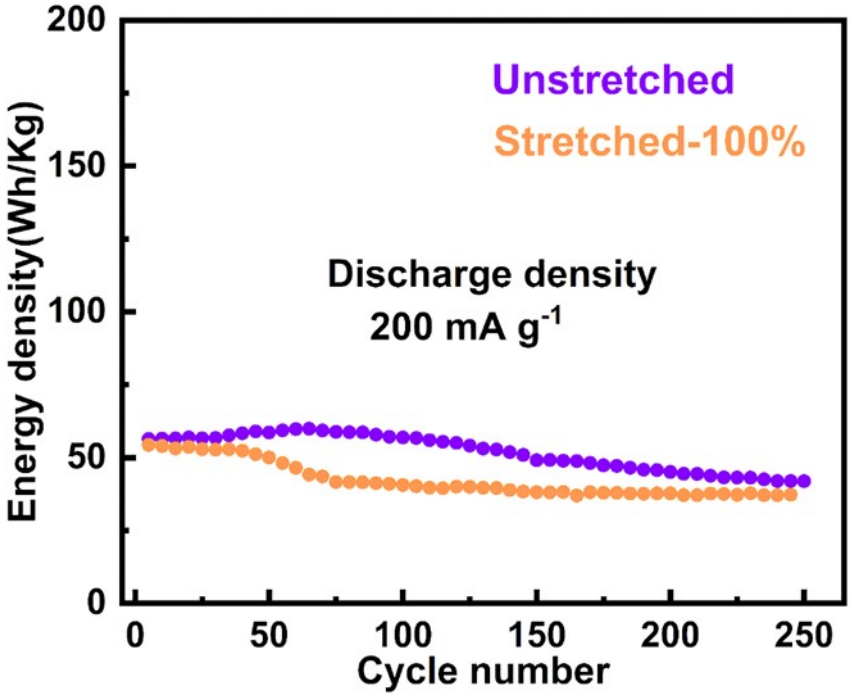

Figure S22. Energy density of the stretchable cell in unstretched and 100% stretched state over 250 GCPL cycles.

The presented stretchable battery provides a considerable capacity and energy density of 102 mAh g^{-1} and 41 Wh kg^{-1} after 250 cycles with a maximum capacity of 115 mAh g^{-1} and 60 Wh kg^{-1} energy density in unstretched state; and the capacity and energy density of the 100% stretched battery can be reached 117 mAh g^{-1} and 52 Wh kg^{-1}, with capacity and energy density of 105 mAh g^{-1} and 37 Wh kg^{-1} after 250 cycles, respectively.

14. Rate performance of the stretchable cell at different current density

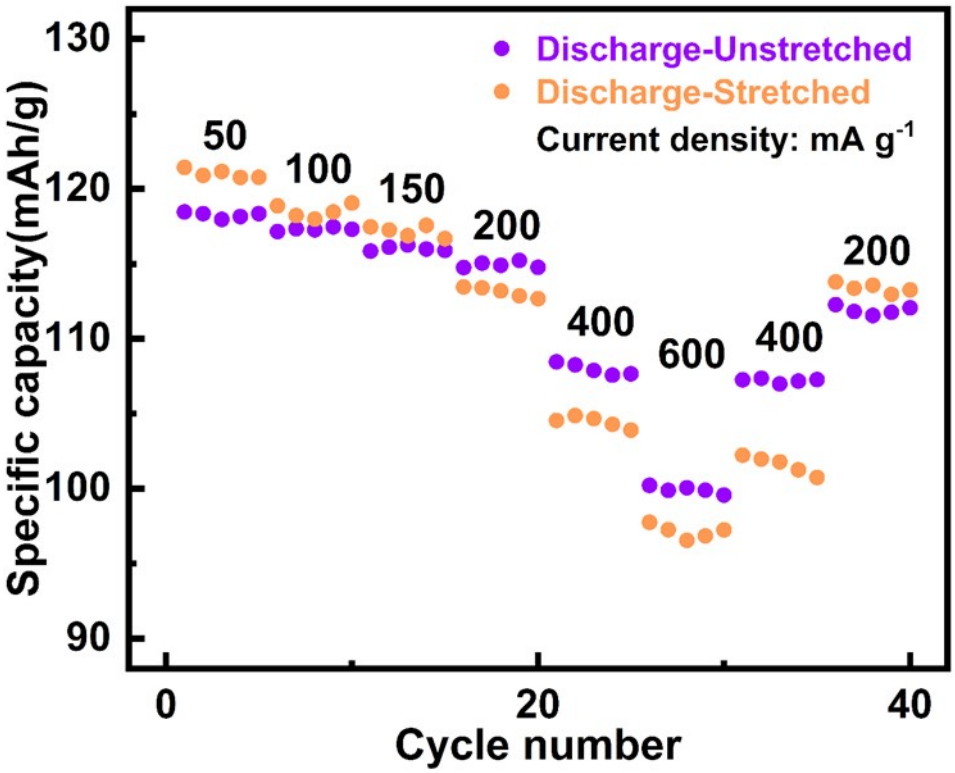

Figure S23. Rate performance of the stretchable cell under stretched and unstretched state at different current densities.

The unstretched state FSSLIB exhibits the reversible capacities of 118.4, 117.1, 115.8, 114.6, 107.8, and 99.8mA h g^{-1} at the current densities of 50, 100, 150, 200, 400, and 600 mA g^{-1}, respectively. When the current density is returned to 200 mA g^{-1}, the specific capacity can be back to 111.2 mA h g^{-1}. And the stretched battery also performed the reversible capacities of 121.4, 118.2, 116.8,

113.4, 104.6, and 96.8 mA h g^{-1} at the current densities of 50, 100, 150, 200, 400, and 600 mA g^{-1}, respectively. After the current density is returned to 200 mA g^{-1}, the specific capacity can be back to 109.2 mA h g^{-1}, demonstrating that the full cell has an excellent reversibility. As shown in Fig. S23, the battery under stretched state shows better specific capacity at low current density, and the unstretched battery exhibits better specific capacity at high current density.

Table 4. Comparison of previously reported intrinsically stretchable cells with our presented stretchable battery.

Current Collector	Active Materials	Electrolytes	Cycle Life	Stretchability	Separator	Reference
Ag-NWs/PAM	LMO//V_2O_5	PAM-WiS	88% (104 mAh/g) after 200 cycles	110 mAh/g for 200 cycles at 100%	◊	Our work
AuNSs/Ag flake Composite	LMO@CNT// PI@AC	$Li2_SO_4$ liquid	89% (96 mAh/g) at 2000 cycles	91.8mAh/g for 30 cycles at 100%	√	[3]
Ag flake/SES	LMO//V_2O_5	PAM-WiS	53% (43 mAh/g) after 50 cycles	39 mAh/g for 50 cycles at 50%	◊	[4]
Au NPs/PU/ GAP	LMO@CNT// PI@CNT	Li_2SO_4 liquid	96% (96 mAh/g) after 1000 cycles	72 mAh/g for 10 cycles at 30%	√	[5]
CNT/CB/SIS	LMO@CNT// PI@AC	Li_2SO_4 liquid	93% (83 mAh/g) after 500 cycles	71 mAh/g for 10 cycles at 30%	√	[6]
Metal Tap (Al/Ni)	LMO@CNT// PI@AC	$LiPF_6$ /EC/PC liquid	93%(97mAh/g) after 200 cycles	88 mAh/g for 30 cycles at 100%	√	[7]
Au SLIC	LFP//LTO	LiTFSI	89% (97 mAh/g) after 50 cycles	97 mAh/g for 50 cycles at 50%	◊	[8]
PAM-CNT	LMO//LTP	PAM/LiCl	65% (43 mAh/g) after 50 cycles	Bend only	◊	[9]
Graphene-CNT/LFP// Graphene-CNT/LTO	LFP//LTO	PVDF-HFP gel/$LiPF_6$	96% (124 mAh/g) after 100 cycles	110 mAh/g for 500 cycles at 50%	√	[10]
Al//Cu foils	LCO//Graphite	EC/DEC/$LiPF_6$ liquid	98% (144 mAh/g) after 20 cycles	140 mAh/g for 50 cycles at 22%	√	[11]
SnO_2/C-Nanofibers// LFP/C-Nanofibers	LFP//SnO_2	EC/DEC/$LiPF_6$ liquid	99.6% (137mAh/g) after 5 cycles	127 mAh/g for 5 cycles at 30%	◊	[12]

References

[1]. Ye, T., et al., A Tissue-Like Soft All‐Hydrogel Battery. Advanced Materials, 2021: p. 2105120.

[2]. Liu, J., et al., Functional hydrogel coatings. Natl Sci Rev, 2021. 8(2): p. nwaa254.

[3]. Song, W., et al., Stand-Alone Intrinsically Stretchable Electronic Device Platform Powered by Stretchable Rechargeable Battery. ADVANCED FUNCTIONAL MATERIALS, 2020. 30(50): p. 2003608.

[4]. Chen, X., et al., Fully Integrated Design of a Stretchable Solid‐State Lithium‐Ion Full Battery. Advanced Materials, 2019. 31(43): p. 1904648.

[5]. Gu, M., et al., Stretchable batteries with gradient multilayer conductors. SCIENCE ADVANCES, 2019. 5(7): p. eaaw1879.

[6]. Song, W., et al., Jabuticaba-Inspired Hybrid Carbon Filler/Polymer Electrode for Use in Highly Stretchable Aqueous Li-Ion Batteries. Advanced Energy Materials, 2018. 8(10): p. 1702478.

[7]. Shin, M., et al., Highly Stretchable Separator Membrane for Deformable Energy-Storage Devices. ADVANCED ENERGY MATERIALS, 2018. 8(23): p. 1801025.

[8]. Mackanic, D.G., et al., Decoupling of mechanical properties and ionic conductivity in supramolecular lithium ion conductors. Nature Communications, 2019. 10(1): p. 5384.

[9]. Kang, S., et al., Stretchable Lithium-Ion Battery Based on Re-entrant Micro-honeycomb Electrodes and Cross-Linked Gel Electrolyte. ACS Nano, 2020. 14(3): p. 3660-3668.

[10]. Shi, C., et al., Accordion-like stretchable Li-ion batteries with high energy density. Energy Storage Materials, 2019. 17: p. 136-142.

[11]. Lu, Y., et al., Stable Cycling of Lithium Metal Batteries Using High Transference Number Electrolytes. Advanced energy materials, 2015. 5(9): p. 1402073-n/a.

[12]. Kwon, O.H., et al., Porous SnO2/C Nanofiber Anodes and LiFePO4/C Nanofiber Cathodes with a Wrinkle Structure for Stretchable Lithium Polymer Batteries with High Electrochemical Performance. Adv Sci (Weinh), 2020. 7(17): p. 2001358.